Questo documento contiene la versione iniziale presentata all'editore dell'articolo

First estimate of wind fields in the Jupiter polar regions from JIRAM-Juno images

D. Grassi[1], A. Adriani[1], M.L. Moriconi[2], A. Mura[1], F. Tabataba-Vakili[3], A. Ingersoll[4], G. Orton[3], C. Hansen[5], F. Altieri[1], G. Filacchione[1], G. Sindoni[1], B.M. Dinelli[6], F. Fabiano[6], S. J Bolton[7], J.E.P. Connerney[8], S. Levin[3], S.K. Atreya[9], J.I. Lunine[10], T. Momary[3], F. Tosi[1], A. Migliorini[1], G.Piccioni[1], R. Noschese[1], A. Cicchetti[1], C. Plainaki[11], A. Olivieri[12], D. Turrini[1,13], S. Stefani[1], R. Sordini[1], M. Amoroso[12]

1. Istituto di Astrofisica e Planetologia Spaziali – Istituto Nazionale di Astrofisica, Rome, Italy

2. Istituto di Scienze Atmosferiche e del Clima, Consiglio Nazionale delle Ricerche, Sede di Roma, Italy

3. Jet Propulsion Laboratory, California Institute of Technology, Pasadena, California, USA

4. California Institute of Technology, Pasadena, California, USA

5. Planetary Science Institute, Tucson, Arizona, USA

6. Istituto di Scienze Atmosferiche e del Clima, Consiglio Nazionale delle Ricerche, Sede di Bologna, Italy

7. Southwest Research Institute, San Antonio, Texas, USA

8. NASA Goddard Space Flight Center, Greenbelt, Maryland, USA

9. University of Michigan, Ann Arbor, Michigan, USA

10. Cornell University, Ithaca, New York, USA

11. Agenzia Spaziale Italiana, Sede di Roma, Italy

12. Agenzia Spaziale Italiana, Sede di Matera, Italy

13. Departamento de Fisica, Universidad de Atacama, Copiapò, Chile

* Corresponding author: davide.grassi@iaps.inaf.it

Abstract

We present estimates of wind speeds at the ~ 1 bar level over both Jovian polar regions inferred from the 5-μm infrared images acquired by the Jupiter InfraRed Auroral Mapper (JIRAM) instrument on the NASA Juno spacecraft during its fourth periapsis (February 2nd 2017). We adopted the criterion of minimum mean absolute distortion (described in Gonzalez and Woods, 2008) to quantify the motion of cloud features between pairs of images.

The associated random error on our wind speed estimates is 12 m/s in the Northern polar region and 9.8 m/s at the Southern pole.

Most of the polar cyclones previously described by Adriani et al. (2018) present azimuthal asymmetries in wind speeds with respect to the System III coordinate system. However, these

1

asymmetries can often be removed by assuming rigid motion (with wind speeds on the order of a
40   few tens of m/s) of an entire vortex with respect to the System III grid.

Once this correction is introduced, the interior of the vortices presents tangential speeds that
increase linearly with distance from the vortex center. The annulus of maximum speed for the main
circumpolar cyclones is located at approximatively 1000 km from their centers, with peak speeds of
80 to 110 m/s. In at least two cases at the Northern polar region, peak speeds are significantly lower
45   (~50 m/s). Beyond the annulus of maximum speed, tangential speed decreases inversely with the
distance from the center within the Southern Polar Cyclone and somewhat faster within the
Northern Polar Cyclone.

A few areas of anticyclonic motions are identified within both polar regions, but more intense and
of more regular shape in the Northern hemisphere.

50   **Keywords**

Jupiter atmosphere, wind speeds, planetary vortices

1.Introduction

The estimate of wind fields from the tracking of cloud features represents a key tool in constraining
the dynamical behavior of planetary atmospheres. The case of Jupiter is by no means an exception.
55   The global-scale zonal wind profiles have been derived from Cassini Imaging Science Subsystem
(ISS) data acquired during the Jupiter flyby of December 2000 [Porco et al., 2003], while on a
regional scale, wind fields have been derived, among others, for the Great Red Spot [Read et al.,
2006, Choi et al., 2007, Asay-Davis et al., 2009] and hot spots and plume areas [Hueso and
Sánchez-Lavega, 1998] on the basis of Voyager, Galileo and Hubble Space Telescope data. Barrado-
60   Izagirre et al., [2008] focused their attention on circumpolar regions at latitudes below 80°, where
longitudinal variations appears to be caused by Rossby waves.

However, very limited information on polar regions beyond the 80° latitude was available prior to
2016. Ground-based observations are adversely affected by high viewing angles, a factor difficult to
mitigate due to the very small axial tilt of the planet. Furthermore, the trajectories of Voyager,
65   Cassini, Galileo and New Horizons spacecraft through or in the Jupiter system remained rather
close to Jupiter's equatorial plane, resulting in similar viewing limitations. Pioneer 11 passed over
the north pole of Jupiter, but could not measure winds due to limitations in the imaging system and
to the very large distance of the observations. On July 4th, 2016 the Juno spacecraft entered into a
polar orbit around Jupiter, providing the opportunity to acquire the best view of its polar regions
70   achieved so far [Bolton et al., 2017]. Among the Juno instruments, the Jupiter InfraRed Auroral
Mapper (JIRAM) [Adriani et al., 2014] is proving particularly useful in studying the upper
troposphere at high latitudes. The instrument includes an IR-imager channel equipped with a broad-
band filter centered at 4.8 μm. This wavelength region allows one to cover simultaneously the day
and night side of the polar regions, enabling synoptic coverage of large areas not achievable by
75   observations acquired at shorter wavelengths dominated by reflected sunlight. The 4.8-μm region
hosts an important transparency window of the gaseous absorption spectrum. In absence of clouds,
the ultimate source of opacity is represented by the H_2 collision-induced absorption and observed
thermal radiation emerges from a pressure level calculated to be about 5.5 bars [see discussion in
Grassi et al., 2017]. The absence of clouds above the 5-bar level is, however, a condition very rarely

2

seen: globally, averaged equilibrium thermodynamics models predict several different cloud layers of ammonia, ammonium hydrosulfide and water, extending over several tens of kilometers in altitude [Atreya et al., 1999]. The analysis of Galileo Near Infrared Mapping Spectrometer (NIMS) spectra by Irwin et al., 2001 found that changes in brightness at 5 μm - at least at the low and intermediate latitudes considered in their study - are correlated not with variability of the higher ammonia cloud, but rather with opacity variations associated with cloud layers between 1 and 2 bars of pressure. In the subsequent discussion, we will assume that features observed in JIRAM images reside in this particular pressure range.

The overall morphologies of north and south poles of Jupiter as seen by JIRAM and by the JunoCam instruments were described by Adriani et al., [2017]. In the current work we adopt the features nomenclature presented in that paper; a suffix 'n' or 's' is added where needed to distinguish northern and southern features. The north pole hosts a central vortex that rotates counterclockwise. Given its location in the northern hemisphere it will be considered a cyclone, with a local pressure minimum at its center. This cyclone shows a low infrared brightness (suggestive of relatively thick cloud coverage), with sizes of turbulent eddies developed down to the smallest scales resolved in the images (about 12 km). This structure is labeled as NPC (as for 'North Polar Cyclone') in Figure 1a. NCP is surrounded by four additional, equally spaced, cyclones, all of which have centers at latitude 83.3°. Three of these cyclones present internal features (approximately within 1000 km from respective centers) with turbulent eddies with sizes down to few tens of kilometers (among them, CPCn2 and CPCn4, where CPC stands for 'Circum-Polar Cyclone'), while the fourth (CPCn8 of Adriani et al., [2017], located at 135°W, not shown in Figure 1a) has a central part with a more 'laminar' aspect, with eddy scales appearing to be limited to at least 100 km. Four other equally spaced cyclones with centers at 82.5° and spaced 45° from the first set of four complete the north pole dynamical organization (among them, CPCn3 and CPCn7). The external four cyclones again present a 'laminar' aspect, with an apparent lack of small-scale eddies in their centers . The south pole presents a slightly more complex morphology. A central 'laminar' vortex (SPC in Figure 1b, as for 'South Polar Cyclone') is surrounded by five vortices irregularly spaced and of different appearance. All six main vortices of the south pole rotate in cyclonic motions(clockwise in the southern hemisphere), suggesting low-pressure centers. While all cyclones show turbulent external parts, with eddies developed at a variety of scale lengths, only three vortices (CPCs 4, 5 and 1) have low-brightness, turbulent centers with eddies of the size of few tens of kilometers, while the remaining two (CPCs 2 and 3, the former not shown in Figure 1b) present 'laminar' central parts. Adriani et al. [2017] presented preliminary estimates of tangential speeds of the polar vortices observed by JIRAM. In the current paper, we substantially extend those findings, presenting the wind fields derived over large continuous areas of both polar regions by a fully automated algorithm. We use JIRAM images acquired during the fourth Juno close passage ("perijove") (PJ4) on February 2nd 2017, the most recent flyby for which sufficient numbers of image pairs are available for wind speed computations.

2. Materials

The JIRAM instrument [Adriani et al., 2014] includes a spectrometer and two image channels operating in different spectral regions. In this paper, we will focus our attention solely on one of these channel (the so called M-filter), where images are acquired by integrating the incoming

radiance over the 4.54- 5.03 μm range. Images have a size of 432 x 128 pixels. All image pixels are acquired simultaneously, i.e.: the bi-dimensional image is formed directly on the focal plane and not by the stacking of consecutive lines in a push broom scan. The field of view of individual pixels is about 240 μrad.

Juno is a spin-stabilized spacecraft and JIRAM acquires one image at each Juno spacecraft rotation (2 rpm). JIRAM pointing has only one degree of freedom, and the pointing can be set only along the maximum circle orthogonal to the spin axis. The Juno spin axis is kept pointed toward the Earth and, therefore, roughly toward the Sun. Moreover, the Juno orbital plane is approximately orthogonal to the spacecraft's spin axis. As a consequence of these constraints, JIRAM images acquired near the close approach are often placed very close to the planet terminator. In most circumstances, JIRAM is operated to acquire a set of consecutive images (a "sequence"), spaced as to create an almost spatially continuous mosaic over a given region.

Figure 1 provides two examples of mosaics created with images from individual sequences.

During PJ4, JIRAM acquired 21 sequences of 13 images each over the north pole and 6 sequences of 19 images each over the south pole. The time interval between two consecutive sequences was 16 minutes over the north pole and 20 minutes over the south pole. The very best pixel spatial resolution at the reference 1-bar level varies from 100 to 9.6 km because of the high eccentricity of Juno's orbit. Similarly, the mean emission angle within a given sequence varies from 75° to 3°. In the analysis presented here we considered only the sequences with a spatial resolution better than 40 km. An exception to this rule was made for sequence 170202_144131, to get at least three sequences over the south pole. The emission angle also needs to be limited, to cope with uncertainties on the radiance emission angle correction in these unexplored cloud conditions. The limit was arbitrarily set to 40°.

Table 1 lists the sequences selected for this study.

Name	Pole	Pixel resolution range (km)	Emission angle range (degrees)	Number of images
170202_114231	N	28.1-27.7	17.13-37.14	12
170202_115039	N	24.6-23.7	12.10-31.38	12
170202_115846	N	21.2-19.7	5.36-24.50	12
170202_120653	N	17.9-15.8	3.22-15.67	12
170202_121429	N	15.6-12.4	2.83-25.93	12
170202_122236	N	17.7-9.6	20.80-68.95*	12
170202_140125	S	21.6-25.8	3.57-19.10	19
170202_142113	S	30.5-33.2	4.47-24.08	19
170202_144131	S	39.8-41.22	10.46-35.15	19

Table 1: summary of JIRAM M-filter image sequences considered for this study. For each sequence, we list the range of mean pixel resolution and mean emission angle (as computed within individual images) found in the sequence. The sequence file name encodes the mean acquisition

4

time of images according the scheme: yymmdd_hhmmss.

*Some images exceeding the 40° mean-emission angle limit were excluded from analysis.

Geometric parameters of each image (geographic locations of pixel corners and centers, solar zenith, emission and phase angles, slant distance, etc.) were computed by means of the SPICE Toolkit [Acton, 1996, Action et al., 2017] on the basis of the re-constructed kernel files available at https://naif.jpl.nasa.gov/pub/naif/JUNO/kernels/. The nominal pointing uncertainty of JIRAM images is about one pixel, translating into minimum pointing uncertainties of about 12 km for the data considered in this study.

3. Methods

The winds were estimated by tracking the motions of different atmospheric features (clouds) over frames acquired at different times. This method relies on the assumption that changes in feature positions are caused solely by the motion of air parcels instead of other phenomena such as condensation/sublimation (notably, due to the propagation of waves).

The wind motions were tracked by minimizing the mean absolute distortion (MAD), as defined in eq. 8.2-37 of Gonzales & Woods [2008]. The method compares two images taken at different times. Firstly, the images are re-interpolated over a common bi-dimensional sampling grid (in our case, with a uniform sampling step of 11.6 km in both spatial directions, corresponding to 0.01 degrees in latitude). Then, *for a neighborhood of each point of the first image,* the MAD algorithm finds the bi-dimensional displacement vector that better matches what is observed in the second image. This allows one, on the basis of the time elapsed between acquisitions, to compute a bi-dimensional speed vector for each point of the first image, creating therefore a 'speed field'. From here on we will use the term 'amplitude' to indicate the length of a speed vector. Further details are provided in Appendix 1.

The estimate of displacements between images are performed in terms of integer numbers of sampling steps along both axes. This implies a minimum detectable motion of 1 sampling step (11.6 km). For images acquired 16 minutes apart – such as the north pole pairs presented in section 4 - this corresponds to a minimum detectable speed of 12 m/s; this value reduces to 9.6 m/s for the south pole pairs acquired 20 minutes apart. These values represent the expected amplitude of random error on our wind estimates, that affects independently each point of the retrieved speed fields.

Conversely, systematic speed errors are those affecting by the same amount the entire velocity field computed from a given pair of images, adding a uniform (over space) unknown vector in the retrieved velocity field. They are mostly caused by the limited precision achievable in pointing reconstruction.   Eventually, pointing uncertainties on re-interpolated images can produce apparent shifts of atmospheric features over the assumed geographical grid - and therefore additional spurious components in speed fields - even in the absence of any intrinsic air parcel motion. Exploiting the large degree of spatial overlap between individual images inside each of the sequences listed in table 1, we were able to develop a method to compare the speeds retrieved from different pairs of images and to remove at least the *relative* differences in the systematic errors

5

185   between different parts of the mosaics of speed maps. Details are provided in Appendix 2.

The six north-pole sequences were arranged in pairs, in order to achieve a time gap around 16 minutes between the selected components of a pair. Pairs with a shorter time gap would have a correspondingly greater minimum detectable wind speed (24 m/s for the 8-minute case). Pairs with a longer time gap would require computational times for the MAD algorithm exceeding our

190   currently available capabilities. Moreover, longer time intervals also increase the possibility of occurrence for phenomena that can not be accounted for by the MAD algorithm, such as small-scale rotations and changes of the cloud patterns due to wave activity. For the three south pole sequences, the only options were pairs with a time gap around 20 minutes between the selected components.

Table 2 details the sequence pairs used for speed fields determination.

Field name	First component	Second component	Correction on x component of speed (m/s)	Correction on y component of speed (m/s)
N1	170202_114231	170202_115846	-14	0
N2	170202_115039	170202_120653	-33	-1
N3	170202_115846	170202_121429	-28	4
N4	170202_120653	170202_122236	-30	1
S1	170202_140125	170202_142113	18	4
S2	170202_142113	170202_144131	18	15

Table 2. Details of velocity fields presented in this study. The source JIRAM sequences are listed for the first and second component used for motion tracking. The last two columns provides the systematic corrections on x and y components of speed deemed necessary to make the central vortex axially symmetric (see section 4 for details).

195

4. Results

The retrieved velocity field for the N1 case – in reference to the System III coordinate system - is shown in Figure 2.

A first notable feature is the azimuthal variation of the velocity amplitude around the NPC centre

200   (approximatively located at [89.5°N, 130°E]), that tends to diminish considerably along the 0° longitude meridian and to increase along the 180° longitude meridian. In each point within 2 degrees latitude from NPC centre, the direction of wind remains essentially orthogonal to the line joining the considered point with V1 centres, with no significant radial components, making it unlikely that local decreases/increases of wind speeds are related to a Rossby wave. On the other

205   hand, visual inspection of NPC cloud features as imaged by JIRAM (Figure 3) demonstrates a remarkable degree of axial symmetry (in terms of typical signal amplitudes and frequency of variations at fixed distance from the centre) up to about 1700 km from NPC centre. Moreover, the wind direction in regions of low velocity amplitude around NPC (namely, those about the 87° latitude circle) as seen in Figure 2b appears to be systematically oriented toward the approximately

210   90°W meridian (negative x direction).

These facts possibly can be explained assuming the existence of a systematic component in the retrieved speed field presented in Figure 2. This component would be a single bi-dimensional vector, uniform over the speed field or at least in large areas around NPC and approximatily oriented along the x-axis. It should be stressed that this systematic component can be caused by a pointing error or by an actual motion of NPC with respect to the System III coordinate or by a combination of the two. Ideally, its removal from the retrieved field should be able to compensate at the same time systematic directions observed in weak wind areas as well as the azimuthal speed asymmetry around NPC centre. This latter feature is particularly desirable, since azimuthal symmetric speed fields can more easily justify the long-time persistence of NPC, that was again observed with similar size, position and appearance in JIRAM images from PJ5 and PJ6.

In practical terms, the removal of the systematic component consists in the subtraction of a uniform velocity vector (a pair of uniform components along x and y axes) from the entire velocityfield returned by the procedure described in Appendix 2, without the introduction of any additional rotation or further transformation.

The criterion adopted to compute the systematic component was the maximization of axial symmetry of velocityamplitudes around NPC, upon removal of the searched component from the original speed field. This was achieved by minimizing the total standard deviation of the speed amplitude, as computed over several annuli around the apparent NPC centre up to a distance of about 1500 km. This method is formally equivalent to searching, in each annulus, for the systematic component that, upon subtraction, brings the velocity amplitudes as close as possible to their mean value. This symmetrization procedure - that introduces a (uniform over the field) correction of the speed field - has been exploited extensively in our subsequent analysis to determine the mean vortice's motions with respect to System III. Notably, the symmetrization procedures relies on a large number of independent wind speed estimates around the vortex center and therefore exploits correlations among independent measurements. Numerical tests have demonstrated that variations in the order of 2.5 m/s on the systematic component to be removed are enough to introduce detectable variations in the derived total standard deviation of the speed amplitudes used to estimate the degree of azimuthal simmetry.

The removal of the component of systematic motion due to the actual motion of NPC with respect to System III is conceptually equivalent to putting oneself in a reference frame, in motion with respect to System III, where the vortex centre remains stationary and the speed field become axially symmetric around that centre.

In the case of field N1, corrections of v_x=-14 m/s and v_y=0 m/s were deemed adequate to make NPC axially symmetric (Figure 4a). This correction is indeed capable of effectively nullifying velocity amplitudes around the 87° latitude. For the other north pole cases N2-N4, the same symmetrization procedure adopted for NPC provided corrections on the x-component of the winds between -33 and -28 m/s and on the y-component of the winds between -1 and 5 m/s. These values are listed in the last two columns of Table 2. We reiterate that these corrections for the N1-N4 cases may include the compensations for a systematic genuine motion of NPC with respect to the System III coordinate system (that must be constant for the different cases, given the short time elapsed between different sequences) as well as for the pointing errors (variable from case to case). Albeit these two effects can not in principle be disentangled and despite the extremely limited statistics (just four cases), we

7

notice that along the x axis we have inferred consistently correction components above the uncertainty level toward the negative direction, suggesting therefore the occurrence of an actual motion of the NPC with respect to the System III coordinates along the 90°W direction.

Figures 4 and A1 present the wind speeds measured over the north pole region in the four available fields, once the removal of systematic components to obtain symmetry for the central pole NPC has been applied to the entire corresponding field. Figure 5 and A2 present the same quantities for the south pole, after symmetrization for SPC.

At the north pole, NPC shows the highest wind speed amplitude of 75 m/s at about 1,000 km from the vortex centre (Figure 6a). The mean relative vorticity – twice the azimuthal velocity divided by the radius – is therefore $1.5 \cdot 10^{-4}$ s^{-1}, which is about half the planetary vorticity at the pole of $3.5 \cdot 10^{-4}$ s^{-1} and of the same sign.

The NPC centre has a clear offset from the nominal Jupiter rotation pole, with offset estimates varying between 0.4 (from photometric estimate of signal symmetry of mosaic 170202_120653) and 0.15 (from location of wind speed minima in N3) latitude degrees. Despite the adopted symmetrization procedure, the wind field retains some asymmetry around speed minima. Namely, the speed peak appears consistently larger in width and slightly lower in peak value along the positive x and y directions (i.e.: along the 135°E meridian). This asymmetry is possibly related to the presence of the small "A" vortex along the 120°E meridian. Wind speed sections from different fields are essentially consistent once the nominal error of 12 m/s is kept in mind.

Among the four internal vortices around NPC, only two (CPCn2 and CPCn4) are covered by our maps. We should note that symmetrization of the wind field for NPC did not lead to axial symmetric velocity fields for these two features, which appear weaker on the east sides for both vortices. Moreover, the velocity patterns in Figures 4 and A1 around CPCn2 and CPCn4 are quite constant from N1 to N4, suggesting that axial asymmetry of CPCn2 and CPCn4 is not an observational artfact. The axially symmetric appearance of both features in JIRAM images as well as their stability over several Juno orbits points again toward the occurrence of relative motions of the two vortices with respect to NPC centre, such that the velocity fields appear indeed axially symmetric in the reference frames moving along their own centres. Moving from this assumption, we repeated the symmetrization procedure described above separately for both CPCn2 and CPCn4 vortices, retrieving the corresponding corrections. Once this correction is subtracted from the correction provided by the symmetrization of NPC, we can infer the net relative velocity of each feature with respect to NPC. This study is best performed in the N1 case, because of the continuous spatial coverage offered by this speed field. Results are reported in Table 3.

	CPCn2		CPCn4	
	Net v_x (m/s)	Net v_y (m/s)	Net v_x (m/s)	Net v_y (m/s)
Field N1	16.	-3.	2	-7.5

Table 3. Motion of CPCn2 and CPCn4 centers with respect to NPC, as derived imposing corrective speed components on wind fields to achieve approximate axial symmetry of wind fields (separately) around each vortex centre.

8

The magnitude of speed of CPCn2 around NPC would imply a rotation period of about $3 \cdot 10^6$ s, i.e: about 85 Jupiter rotation periods or 35 Earth days. However, net speeds of CPCn2 and CPCn4 with respect to NPC are neither oriented along the parallels (i.e.: both have a meridional compoonent) nor consistent with a rigid rotation of the entire pattern of nine northern vortices around the pole, since both cyclones appears to move approximatively toward the 150W meridian . Later JIRAM data acquired during PJ5 and PJ6 clearly indicate that CPCn2 and CPCn4 were still at the same longitudes they occupied during PJ4, demonstrating that detected motions were reversed between PJ4 and PJ5. Unfortunately, it is not possible to verify independently these motions by tracking the centres of vortices over JIRAM images acquired at different times. The large uncertainties on the definition of vortex 'centres', regardless of the adopted method (radiometric barycentres or minima of speed field), implies errors on derived feature speeds much larger than those achieved by speed axial symmetrization. For example, in the NPC case the position of centre can be defined with an uncertainty of 0.15 degrees in longitude: this implies an uncertainty on speeds of 180 m/s for the northern cases listed in Table 3, about an order of magnitude greater than the values reported in Table 3.

The sizes of CPCn2 and CPCn4, as inferred from wind speed fields, are comparable to that of NPC, but absolute peak speeds (even after symmetrization) are considerably lower, reaching about 55 m/s again at about 1000 km from their apparent centers.

The small "A" feature is an anticyclonic feature and presents maximum speeds around 42 m/s. At least four further smaller anticyclonic structures exist around NPC (two are seen Figure 7a and a further one in Figure 7b, marked as "a").

Results on CPCn3 and CPCn7 are more problematic. Firstly, their marginal positions on N1 did not allow a symmetrization to be performed to compensate the joint effects of the motion of the feature with respect to System-III coordinates and of pointing errors. Secondly, significant portions of external rims (beyond 2° from their respective apparent centres, regions hosting both very dark and very bright areas in Figure 1a) are essentially featureless, strongly limiting the validity of MAD motion tracking. Despite these limitations, some results are robust: their central parts (at intermediate brightness in Figure 1a) are rich in features, that allow effective tracking of wind speeds. The fastest annulus on CPCn3 at about 1000 km from cyclone center shows speeds in the range 100-110 m/s. The mean relative vorticity is therefore around $2 \cdot 10^{-4}$ s^{-1}, to be compared against a planetary vorticity at 82.5° of $3.47 \cdot 10^{-4}$ s^{-1} and of the same sign. Coverage of CPCn7 is less complete and the area corresponding to the high-speed annulus in CPCn3 is not included in N1. Nevertheless, the region where estimates are available is already suggestive of much higher speeds than the ones observed in NPC, CPCn2 and CPCn4. An interesting feature associated with CPCn3 is located at [85°N, 90°E] where velocity maps, supported by visual inspection, demonstrate how the flow is strongly accelerated (Figure 7b, marked as "f"), moving from the stagnant regions at [83°N, 105°E].

Over the south pole, symmetrization of velocity fields around SPC provided - for both the S1 and S2 cases - correction values that once extended to the entire corresponding speed field provided rather symmetric values also around the centres of CPCs3, CPCs5 and CPCs1. The symmetrization procedure for the two cases S1 and S2 returned similar corrections, possibly suggestive of an overall motion of most of the south pole six vortices pattern toward the approximate direction of

9

60°E. The amplitudes of the corrections are, however, rather small once compared to the expected systematic uncertainties on speed determination due to the pointing, and consequently the values reported in Table 2 should actually be interpreted as upper limits for the overall motions of south pole vortices. Notably, the computation of total standard deviation of the velocity amplitudes - implied by the symmetrization procedure - was limited to distances from nominal SPC center entirely covered by available velocity maps, to avoid biases related to vicinity of image borders.

It should be noted that even a simple visual inspection of Figure 1b demonstrates the asymmetric nature of SPC: its central part appears clearly elongated along the 150°E meridian and its centre shows an offset of about 1.5° from the nominal south pole. It is therefore not surprising to observe a residual asymmetry of speed amplitudes even after the symmetrization of speed amplitudes had been performed at the best degree allowed by the removal of a uniform vector in the entire SPC region. With comparison to NPC, the speed sections (Figure 6b) present higher peaks values (up to 90 m/s at 1,000 km from the centre), and a slightly higher relative vorticity of $1.8 \cdot 10^{-4}$ s^{-1}.

CPCs4, even after an attempt to symmetrize separately speed amplitudes around its apparent centre, shows a very peculiar structure, with two arms at moderate speed (approximately 55 m/s, indicated by "m" in Figure 5a) apparently embracing a relatively stagnant area at [84°S, 25°W] ("s" in Figure 5a). Larger images of the same area strongly suggest that the upper arm is associated with an apparent acceleration of the flow from an area located at [80°S, 45°W] (just west of area "J" in Figure 4 of Adriani et al. [2017]).

CPCs5 presents the highest wind speeds observed in Jupiter polar vortices, exceeding 115 m/s. No evident high speed arms were detected for this vortex, as well as for CPCs1, despite their morphological resemblance (very opaque centre) with CPCs4. CPCs3 presents some small scattered areas of apparent low speed along its high-speed annulus (seen as blue specks within CPCs5 in Figure 5a), but these turned out to be associated with featureless regions in Figure 1b and are therefore likely related to MAD algorithm failures.

The south polar region presents a number of other interesting features. An irregular ribbon of moderate wind (55 m/s) exists around [83°S, 15°E] (rightmost "r" label in Figure 5a), surrounding a very opaque area centred at [81°S, 15°E]. In the entire region, winds appear to rotate clockwise, as observed for the main southern vortices (CPCs) described above. Figure 7c provides further details of the area (a part of the ribbon is marked there as "r"). A second similar ribbon exists between 30°E and 45°E (leftmost "r" label in Figure 5a). Both ribbons represents likely the southern parts of highly distorted cyclonic structures, only partially covered in our velocity maps, possibly smaller versions of the folded filamentary regions reported in Orton et al, 2017 at lower latitudes in JunoCam data. p to 50 m/s

A number of small anticyclones, with very opaque centres, are observed at [85°S, 130°W], [82°S, 40°W] (also visible in Figure 7c and marked there as "a") and [81°S, 175°W]. The small bright feature with a more opaque centre at [82.5°S, 125°W] also appears to be an anticyclone. Extremely weak anticyclonic circulation is tentatively identified in two regions with low wind speeds (<20 m/s) between SPC, CPCs5 and CPCs4 (Figure 7d, marked as "a?"), but with patterns much less defined in comparison to what is observed around NPC.

10

5. Discussion

370 Considering as reference the NPC centre, after symmetrization the speed field in the region within 3000 km is essentially tangential, i.e. detected radial motions are comparable with the estimated speed error. To get insight on the nature of the motion, we can consider the Rossby number R_o. For a circular vortex at the pole, R_o is the ratio of the centripetal acceleration to the Coriolis acceleration

$$R_0 = \frac{-\frac{v^2}{r}}{2\Omega v} \quad [1]$$

375 r being the distance from vortex center. For the NPC, v = 75 m/s and r = 1000 km and one obtains $R_o \approx 0.21$. This means the cyclone is moderately cyclostrophic and the radial force balance in pressure coordinates is

$$-\frac{v^2}{r} - 2\Omega v = -g\left(\frac{\partial z}{\partial r}\right)_P \quad [2]$$

Assuming v is a linear function of r from the center out to 1000 km, the height z of a constant
380 pressure surface at r = 1000 km compared to that at the center is 1280 m. This is about 0.05 times the pressure scale height at the 1-bar level, where the temperature is 165 K.

The NPC has a constant angular speed at least up to 500 km from vortex centres, but no morphological discontinuity is apparent on JIRAM images at this distance, as well as at the speed peak at 1000 km. Beyond 1400 km, once we model the decay of the tangential speed as

385 $$v = C_1 \cdot r^{-\gamma} \quad [3]$$

where C_1 is a constant, we observe ([Figure 8a](#)) that speeds decay more quickly along radius than expected for the case of an irrotational vortex (i.e.: with γ=1). A fit of speed points between 1500 and 3200 km returns a value of γ=1.40±0.04.

The cyclostrophic component remains significant also for the SPC (R_0~0.25), where speed profiles
390 imply an overall variation of approximatively 1600 m of the height of 1-bar pressure level from the annulus of maximum speed to the vortex centre. Also for the SPC case, profiles suggest a constant angular speed up to a distance on the order of at least 500 km from the apparent motion centre. In the SPC case however, the outer ring (beyond 1500 km from nominal centre) displays a trend of speed more consistent with γ=1 over an annulus with a width of at least 600 km (γ=1.06±0.18,
395 from a fit between 2000 and 2600 km). Beyond a radius of 2,600 km, the tangential speed drops more quickly with increasing distance, with γ approaching the valuye of 1.5 ([Figure 8b](#)).

The different behaviours of the NPC and SPC are consistent with their overall morphologies. The NPC shows eddies down to the smallest visible spatial scales over its entire radius. This suggests that turbulence may dissipate energy in a relatively effective manner in the outer parts of the
400 vortices, where speed decay occurs. Conversely, the SPC develops small-scale eddies only beyond 2000 km from the estimated centre. In absence of an effective turbulent dissipation of energy in the region between 1000 and 2000 km from the centre, the profiles remain essentially those expected from a conservative free vortex.

Adriani et al. (2017) observe that the constellation of CPCs is reminiscent of the formation of

11

405   vortex crystals, which have so far only been observed in magnetized plasmas (e.g. Fine et al. 1995) and rotating superfluids (e.g. Campbell and Ziff, 1979). In theory (Schecter et al. 1999), 2d turbulent exchanges can cause an inviscid fluid to relax into vortex crystal structures. According to Schecter et al. 1999, vortices in vortex crystals are stationary compared to a rotating frame of reference, where each vortex and the frame of reference have the same rotation rate. The present

410   paper identifies the rotation periods of the circumpolar cyclones on the order of one Jupiter day, and hence CPCs and the System III coordinate system have similar rotation rates.

While this comparison supports the argument for vortex crystallization at the poles of Jupiter's atmosphere, there remain several unresolved questions. Experimental setups with magnetized

415   electron columns retain their vortex crystal structure for 400 rotation periods (Fine et al. 1995). Continuous polar observations with the JIRAM and JunoCAM instruments on the Juno spacecraft for over a year have shown the CPCs in a stable constellation for over 900 rotation periods. These findings have led to a number of new questions to be addressed by future models, especially 1) What is the source of energy that maintains the circumpolar cyclones beyond the lifetimes of freely

420   relaxing vortex crystals? 2) What parameters differ between the polar atmospheres of Saturn and Jupiter, that one produces a polar hexagon and a single, strong central cyclone at each pole, while the other results in vortex crystallization?

6. Conclusions

425   Results presented here are a first attempt to extract wind fields over large portions of Jupiter polar areas, with random errors in the order of 12 m/s. Data were acquired during a single Juno pericenter passage on February 2nd, 2017.

The two cyclones placed over both poles (NPC and SPC) reach their maximum speeds at about 1,000 km from their respective centers; the southern vortex appears to rotate slightly faster that the

430   northern counterpart (90 m/s and 75 m/s respectively). In the surrounding circumpolar cyclones, speed exceeds 100 m/s in at least three cases (CPCn3, CPCs1, CPCs5). Considering the other cicrcumpolar cyclones included in our maps, the two southern structures (CPCs4 and CPCs3) show sligthly lower maximum speeds (80-90 m/s) while the two northern vortices (CPCn4 and CPCn2) appear considerably slower (about 55 m/s). In all cases, the peak speeds are reached at about 1000

435   km from their respective centers, but in general peaks are rather broad, and therefore the definition of the size of maximum speed ring is prone to an uncertainity of about 500 km.

Central polar vortices in both hemispheres are in moderate cyclostrophic balance and with velocities increasing linearly along radius within 500 km from their centres. In the outer parts of the southern vortex, flow is irrotational in a large annulus (γ=1.06±0.18); in the northern vortex,

440   rotational speed decays along radius faster than expected for irrotational flow (γ=1.40±0.04).

While the main vortices are confirmed to be cyclones, several smaller anticyclonic features are also detected.

We made azimuthal averages around vortex centres, to account both for pointing errors as well as systematic motions of vortices with respect to the System-III coordinates. Despite the ambiguity

445   related to the absolute pointing, both polar cyclones appear to be subject to overall motions with

12

respect to System III, with translation speeds of the vortex centres in the order of 25 m/s for the northern cyclone and slightly less (18 m/s) for the southern cyclone. The stability of vortex patterns over several Juno perijove passages implies, however, that these motions are not constant and may reverse between Juno perijoves.

450

465

13

Appendix 1. Details on the MAD method

470 A monochromatic image such as those produced by JIRAM can be considered as a single-valued function f of the two *integer* variables x and y representing the pixel coordinates, i.e.: the signal measured in the pixel with coordinates x_0 and y_0 is given by $f(x_0, y_0)$.

Let's consider a pair of images f and p, being p derived from f by some kind of motion in the observed scene. For each point (x_0, y_0) in f and each possible bi-dimensional shift vector (dx, dy) we

475 define the mean absolute distortion (MAD) as

$$MAD(x_0, y_0, dx, dy) = \sum_{i=-\Delta x}^{+\Delta x} \sum_{j=-\Delta y}^{+\Delta y} |f(x_0+i, y_0+y) - p(x_0+i+dx, y_0+y+dy)| \quad \text{[A1.1]}$$

Here, $(2 \cdot \Delta x + 1)$ and $(2 \cdot \Delta y + 1)$ are the sides of a square neighborhood of (x_0, y_0) from the first image f that is translated over the second image p by varying the *integer* values of shift (dx, dy). The algorithm defines the motion of the point (x_0, y_0) from f to p as the shift vector (dx, dy) that

480 minimize the MAD function.

In practical terms, once (x_0, y_0) is fixed, the code performs $(2 \cdot \max|dx|+1) \cdot (2 \cdot \max|dy|+1)$ independent estimates of (1) for different (dx, dy) values, selecting eventually the one providing the smaller MAD value. The estimates of best (dx, dy) for different points of f (i.e.:different x_0, y_0) are performed independently for each point.

485 Notably, the usage of the MAD method implicitly requires that f and p both refer to the very same bi-dimensional spatial grid. In our case, original JIRAM images were re-interpolated over an x,y plane on the basis of geographic coordinates of pixel centres (System III coordinates). We adopted an azimuthal equidistant projection centred over the pole of interest with a sampling step of 0.01 degrees of latitude. This value corresponds to about 11.6 km and final images are consequently

490 oversampled of a factor between 1 (no oversampling) and 4 with respect to the original data. An oversampling up to a factor 4 is "typically" used in the MAD method (Gonzales & Woods, [2008]).

The size of the region to be explored in the second image p (i.e.: range of values for |dx| and |dy|) depends upon the expected displacement magnitude. With the re-sampling described above, a maximum shift of 20 points from nominal position along the vertical and horizontal directions (in

495 both senses) would correspond to wind speeds up to 240 m/s for images pair acquired 16 minutes apart (as in the case of north pole observations listed in Table 1), to be compared against the maximum speeds of mid-latitude jets of 150m/s [Porco et al., 2003]. A pair with a longer time gap between members requires correspondingly larger regions to be explored over p, with computational times being proportional to $\max|dx| \cdot \max|dy|$. The values of Δx and Δy (i.e.: the size

500 of neighbourhood for the points of the first image) is set by trial-and-error, but it should be of the order of maximum values for |dx| and |dy|: in our case a side of 20 points was again deemed adequate.

The MAD method allows one to estimate the motion from f to p for each individual point of f, and therefore to obtain full speed fields over the image. The method considers only rigid translations as

505 possible displacements for the neighborhoods of the f points and therefore possible rotations are not

14

included. This limitation requires that time interval between the acquisitions of *f* and *p* shall remains small with respect to any expected rotation period in the observed scene. The sizes of Δx and Δy shall also remain reasonably small, since any rotation occurring at scales smaller than the size of the search neighborhood (but still greater than the sampling step) from the first image would hamper

510   the effectiveness of MAD search.

Albeit from a formal perspective the MAD method can provide a speed vector for each point of *f*, in the practical implementation one shall consider how the intrinsic motion of the scene can bring the neighborhood outside *p*. For implementation simplicity in our code *f* and *p* were cut to the entire available overlap region and speed field were not computed for the points of *f* lying within

515    $\max(\Delta x + |dx|, \Delta y + |dy|)$ from image borders.

Alternatively to MAD minimization, another approach may consist in maximizing the correlation between the neighborhood and the second image. This method however was eventually discarded since direct tests demonstrated its proneness to considerable systematic errors once applied to this specific subset of JIRAM data. The reasons for this behavior are beyond the scope of this paper, but

520   are not surprising when dealing with turbulent motions where fractal-like structures are often observed.

Appendix 2. Mitigation of pointing errors

525   Systematic speed errors are more difficult to assess and may arise from a variety of sources. Notably, JIRAM pointing determination and – consequently – accuracy of geometric parameters of the observations (pixel coordinates) are limited by the precision to which the Juno spacecraft can determine its own phase over the rotation around the spin axis. Briefly, this translates into errors on estimated pixel spatial positions up to 240 µrad (i.e.: the size if 1 pixel) for the original JIRAM

530   images and into errors up to 4 sampling points for the re-interpolated data (once the sampling size of 11.6 km and the maximum allowed spatial resolution of 40 km are considered).

In the estimate of speed fields from JIRAM sequences shall take into account a few specific issues.

1. Different images composing a sequence are not acquired simultaneously. Inside a given sequence, each image is acquired during a different Juno rotation and therefore there is a

535   minimum time interval of 30 second between different acquisition (Figure A3)

2. The systematic pointing error (difference between estimated and actual pixel positions) is not merely unknown but – most important - different in different images.

These two facts preclude the simplistic approach of creating two mosaics of interpolated images (a mosaic from each sequence) and apply the MAD search over these two mosaics. The usage of a

540   mosaic of images is prone to the ambiguity in the definition of acquisition time (that is different in different regions) as well as to *relative* unknown displacements between parts of the mosaic originating from different individual images.

Conversely, we decided to consider each possible pair of JIRAM images with the first image from the first sequence and the second image from the second sequence. The MAD search procedure was

15

545   applied to each of these possible image pairs, to derive the speed field in the overlap region. For
      simplicity, the MAD search was limited to the cases where re-interpolated pairs of images have an
      overlap exceeding 10^4 sampling points.

      Considering now a specific pair of images as described above (first image from first sequence,
      second image from second sequence), the speed field computed in the overlap region is affected by
550   a systematic speed error (δv_x, δv_y), uniform over the entire overlap region, derived from the
      unknown (and different) systematic pointing errors - (δx_1, δy_1) and (δx_2, δy_2) - affecting the two
      images.

$$\delta v_x = \frac{(\delta x_1 + \delta x_2) \cdot s_x}{\Delta t}$$
$$\delta v_y = \frac{(\delta y_1 + \delta y_2) \cdot s_y}{\Delta t} \quad [A2.1]$$

      Here s_x and s_y are the amplitudes of sampling steps along the x and y directions (11.6 km in both
555   cases in our analysis) and Δt the time elapsed between the acquisitions of the two images of the
      pair, a quantity that – contrarily to mosaics - is defined unambiguously for individual images. For
      simplicity, we denote here as 'wind tile' the individual speed field derived from the analysis of a
      given pair of images as described above (first image from first sequence, second image from second
      sequence). Spatial coverage of each wind tile correspond to the overlap area between the two
560   images.

      From now on we do not consider any longer the images or their overlap regions, but only wind tiles
      (speed fields over given areas). The mosaicking of wind tiles retains the ambiguity due to the
      unknown speed errors formally given by (2) that affects in different amount each wind tile. A simple
      stacking of wind tiles makes this issue well evident, with clear discontinuities of speed amplitude at
565   tile borders.

      However, spatial coverage of different wind tiles shows often large areas of overlap. In these cases
      it is possible to consider an arbitrary 'start tile' and to add - one by one - all available tiles exploiting
      the condition that in every point of overlap regions speed amplitudes must be identical in the two
      overlapping tiles (within the approximate random errors described in section 3). In order to met this
570   condition, we assume initially as 'correct' the speeds of the start tile and we look for an additional
      speed vector that, once added to every point of the tile to be added, provides the best match of speed
      amplitudes in the overlap regions. This additional speed vector is the same for every point of the tile
      to be added and is eventually applied also to the points outside the overlap region with the start tile.
      Proceeding with all available tiles, the final 'wind mosaic' is still affected by an unknown systematic
575   (i.e.: uniform over its spatial coverage) *absolute* errors on speed (namely, those affecting the 'start
      tile'), but virtually no *relative* errors between its different parts.

      The method is however subject to some limitations. Each addition of a new tile to the wind mosaic
      requires the determination of a separate corrective speed vector. The precision at which this vector
      can be determined is limited by several factors, including the need to perform the search of the
580   optimal correction over a grid of finite size (¼ of sampling step in our case) and the slightly
      different time gaps used to compute different wind tiles. This latter factor is strictly related to the
      fact that shifts are determined by the MAD algorithm in terms of integer sampling points: different

16

time gaps lead therefore to slight different sets of possible speed values. In general terms, the corrective components applied during mosaicking are capable to reduce the amplitudes of speed discontinuities observed at tile borders to at least 25% of the original values.

All the speed fields discussed in this paper are actually wind mosaics creating according the procedure described above. In all cases, the selected start wind tile was the one exhibiting the most complete coverage on the central vortex of each pole.

Notably, we attempted also an alternative approach consisting in creating mosaics of images from a given sequence where, starting from an initial (re-interpolated) image, we added one-by-one other images introducing, at each addition, a corrective bi-dimensional shift in order to minimize differences in the overlap regions. These corrected image mosaics were eventual fed to the MAD algorithm. Discontinuities at borders in speed field at tile borders were found to be usually of comparable or *greater* magnitude that achieved without any correction, despite being computed for exact elapsed times.

The removal of relative errors between different parts allows one to compare distant spatial regions can not be observed in an individual JIRAM image at adequate spatial resolution. In the present study, this is particularly important for the central regions of different polar vortices. The procedure of mosaicking of 'wind tiles' described above was possible over the entire width of the investigated areas only for the N1, S1 and S3 fields described in table 2. In other cases, gaps exist between different section of the considered mosaic.

17

References

Acton, C. H. (1996), *Ancillary Data Services of NASA's Navigation and Ancillary Information Facility*, Planetary and Space Science, 44 (1), pp. 65-70.

Acton, C.H, et al. (2017), *A look toward the future in the handling of space science mission geometry,* Planetary and Space Science, DOI 10.1016/j.pss.2017.02.013

Adriani, A. et al. (2014), *JIRAM, the Jovian Infrared Auroral Mapper* Space Sci Rev, doi:10.1007/s11214-014-0094-y

Adriani, A. et al. (2018), *Geometric cyclonic patterns in Jovian Polar Regions*, Nature, TBC, doi:10.1038/nature25491

Asay-Davis, X. S., et al. (2009), *Jupiter's shrinking Great Red Spot and steady Oval BA: Velocity measurements with the 'Advection Corrected Correlation Image Velocimetry' automated cloud-tracking method*, Icarus, 203, 164-188, doi: 10.1016/j.icarus.2009.05.001

Atreya, S. K., et al. (1999), *Comparison of the atmospheres of Jupiter and Saturn: deep atmospheric composition, cloud structure, vertical mixing, and origin*. Planet. Space Sci., 47, 1243-62. doi:10.1016/S0032-0633(99)00047-1

Barrado-Izagirre, N., et al. (2008), *Jupiter's polar clouds and waves from Cassini and HST images: 1993-2006*, Icarus, 194, 173-185, doi: 10.1016/j.icarus.2007.08.025

Bolton, S. J., et al. (2017), *Jupiter's interior and deep atmosphere: The initial pole-to-pole passes with the Juno spacecraft. Science*, 356(6340), 821-825, doi: 10.1126/science.aal2108

Campbell, L. J., and Robert M. Ziff (1979) *Vortex patterns and energies in a rotating superfluid* Physical Review B, 20, 1886-, doi: 10.1103/PhysRevB.20.1886

Choi, D. S., et al. (2007), *Velocity and vorticity measurements of Jupiter's Great Red Spot using automated cloud feature tracking,* Icarus, 188, 35-46, doi: 10.1016/j.icarus.2006.10.037

Fine, K. S., et al. (1995) *Relaxation of 2D turbulence to vortex crystals* Physical review letters, 75, 3277-, doi: 10.1103/PhysRevLett.75.3277

Gonzalez, R. C., Woods, R. E. (2008), *Digital image processing, 3rd edition.* Prentice Hall, ISBN 13: 978-0-13-505267-9

Grassi, D., et al. (2017), *Preliminar yresults on the composition of Jupiter's troposphere in hot spot regions from the JIRAM/Juno instrument*, Geophys. Res. Lett., 44, doi:10.1002/2017GL072841.

Hueso, R., and A. Sánchez-Lavega (1998), *Motions in hot spot-plume regions using Voyager images*, Icarus, 136, 353–357, doi:10.1006/icar.1998.6018.

Irwin, P. G. J., et al. (2001), *The Origin of Belt/Zone Contrasts in the Atmosphere of Jupiter and Their Correlation with 5-μm Opacity*, Icarus, 149, 397-415, doi:10.1006/icar.2000.6542.

Lee, D.T., Schachter, B.J. (1980), *Two Algorithms for Constructing a Delaunay Triangulation*, Int. J. of Computer and Information Sci., 9, pp. 219-242.

Orton, G. S., et al. (2017), *The first close-up images of Jupiter's polar regions: Results from the Juno mission JunoCam instrument,* Geophys. Res. Lett., 44, 4599–4606, doi:10.1002/2016GL072443.

Porco, C., et al., (2003), *Cassini imaging of Jupiter's atmosphere, satellites, and rings*. Science, 299 (5612), 1541-1547, doi: 10.1126/science.1079462

Read, P. L., Gierasch, P. J., & Conrath, B. J. (2006), *Mapping potential-vorticity dynamics on Jupiter. II: the Great Red Spot from Voyager 1 and 2 data,* Quarterly Journal of the Royal Meteorological Society, *132*(618), 1605-1625, doi: 10.1256/qj.05.35

Schecter, D. A., et al. (1999) *Vortex crystals from 2D Euler flow: Experiment and simulation* Physics of Fluids, 11, 905-914., doi: 10.1063/1.869961

645

650

170202_114231

170202_140125
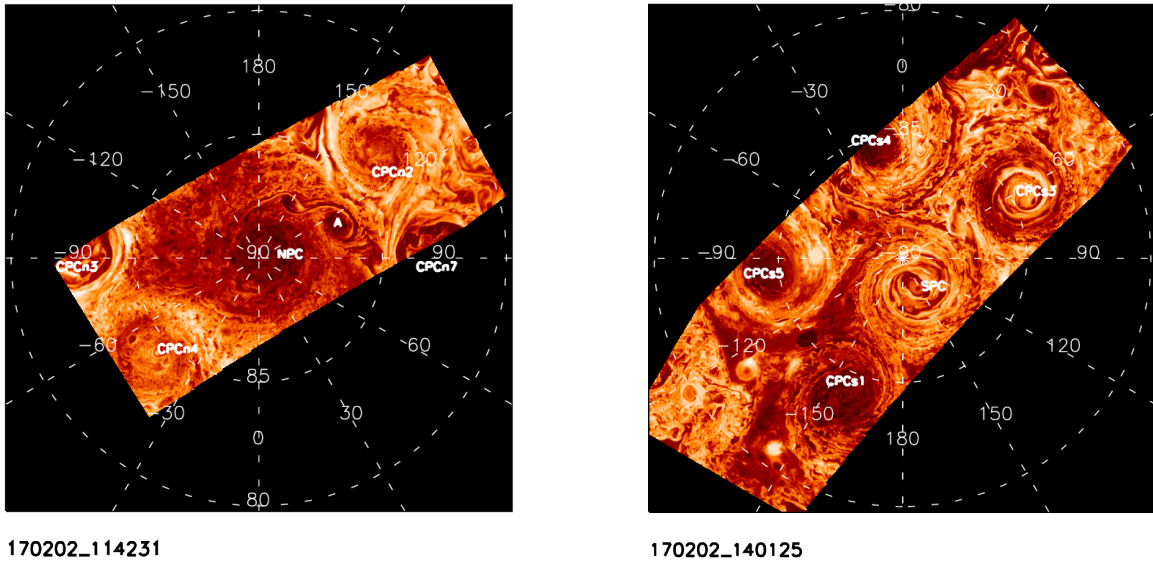
Figure 1. Examples of mosaics composed from spatially interpolated images. Each mosaic contains only images from the JIRAM sequence given in the label. Further details on geometric properties of the observations are provided in Table 1. Labels identify individual features mentioned in the text according the nomenclature adopted in Adriani et al., 2017.

Minimum detectable wind: 12 m/s

a   b
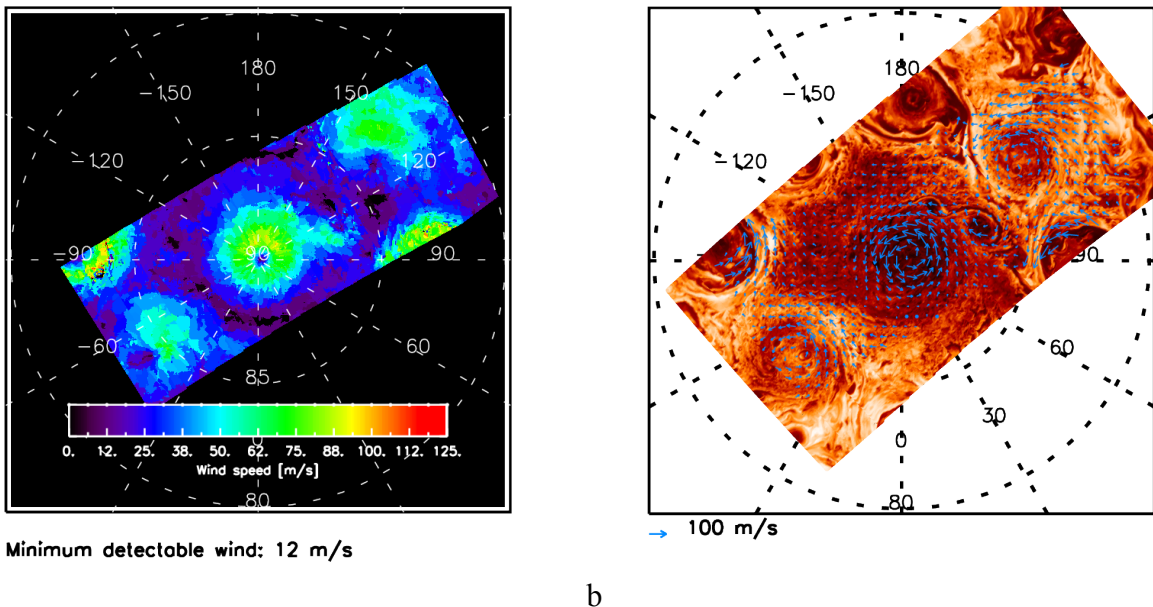
Figure 2: Wind velocity amplitudes (panel a) and directions (panel b) with respect to System-III coordinates, as derived in the N1 case . Background image for the left pane is a mosaic of the original images from the 170202_114231 sequence. Directions are presented only in the areas were overlap with images of sequence 170202_115846 exists.
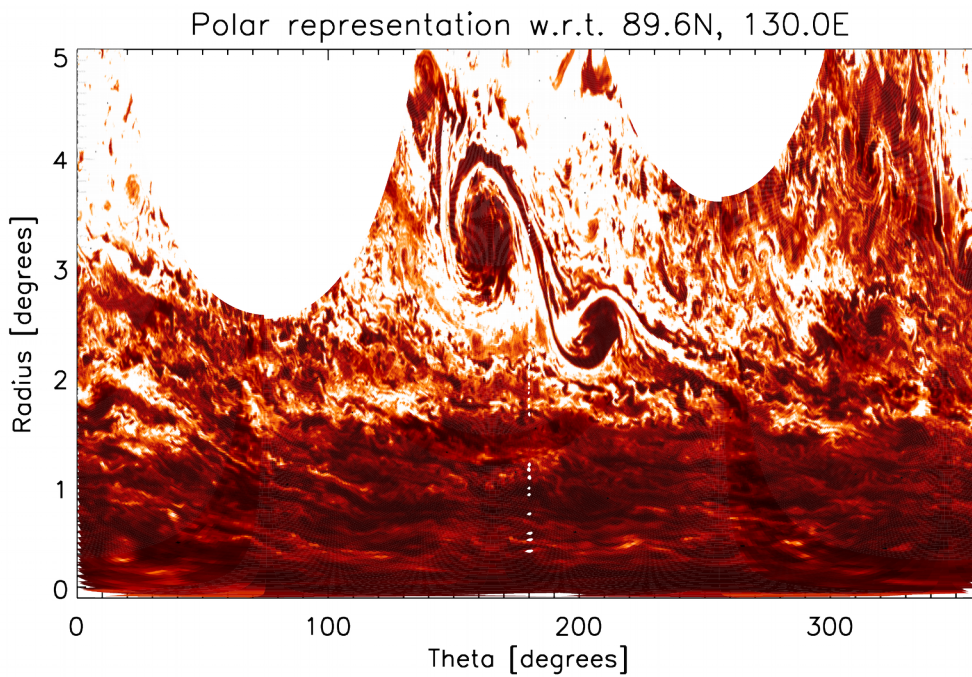
Figure 3. Detailed view of the NPC region from sequence 170202_120653. Data were re-projected as follows: the distance of pixel along the y axis (radius) corresponds to its radial distance from the estimated vortex centre at [89.6°N, 130°E], the distance of pixel along the x axis (theta) corresponds to the angle between the directions pixel-vortex centre and pole-vortex centre. This representation allows one to appreciate the degree of axial symmetry of vortex cloud structure up to at least 1.5 degree from vortex centre (1750 km).

660
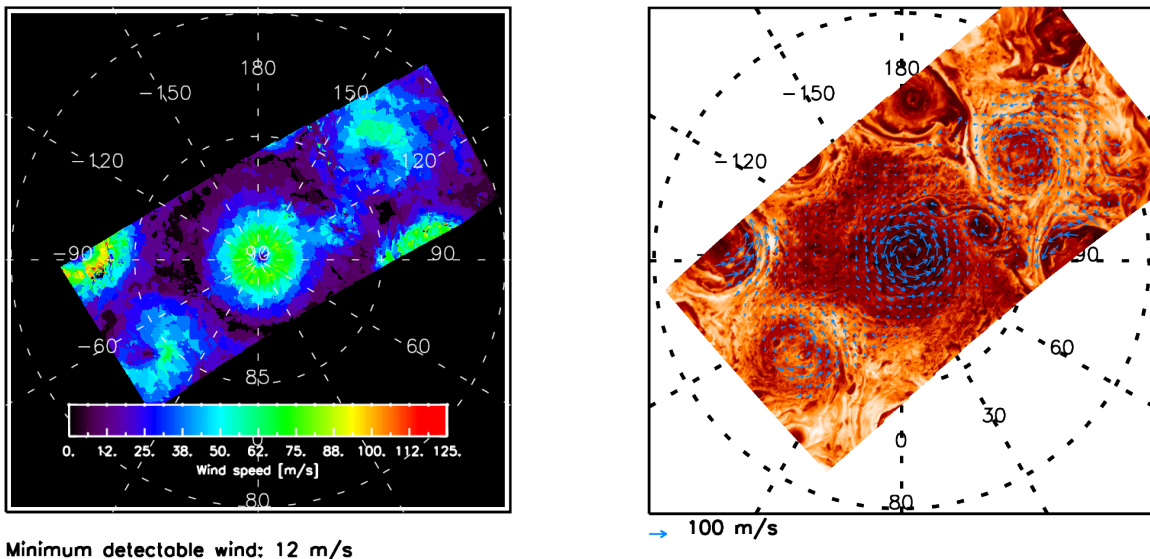
a   b

Figure 4: Wind velocityamplitudes (panel a) and directions (panel b) over the north pole, derived for the N1 case of Table 2, as corrected to achieve maximum azimuthal symmetry of wind speed around the centre of NPC. Figure A1 provides analogous information for cases N2, N3 and N4.

21
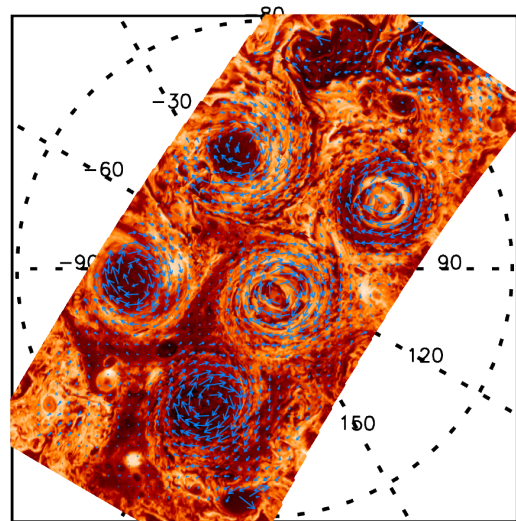
a   b

Figure 5: Wind velocity amplitudes (panel a) and directions (panel b) over the south pole, derived for the S2 case of Table 2, as corrected to achieve maximum azimuthal symmetry of wind speed around the centre of SPC. Labels "m", "s" and "r" indicate specific features discussed in the text. Figure A2 provides analogous information for case S1.
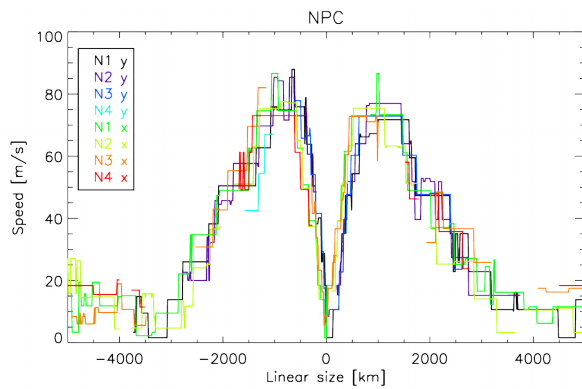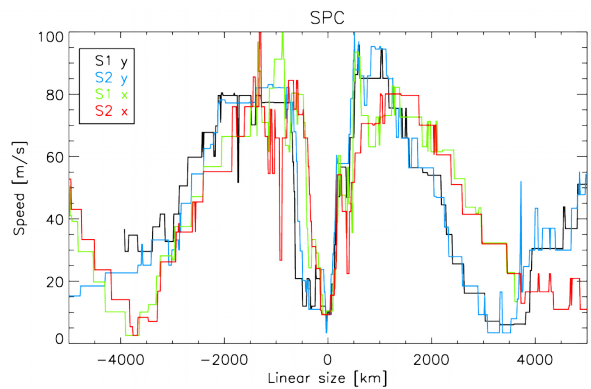
a   b

Figure 6. Cross sections of wind velocity amplitudes fields along the x and y directions of Figure 1 for the central vortices over the north (panel a) and south (panel b) poles. Different colours are for different cases listed in table 2 and different directions.
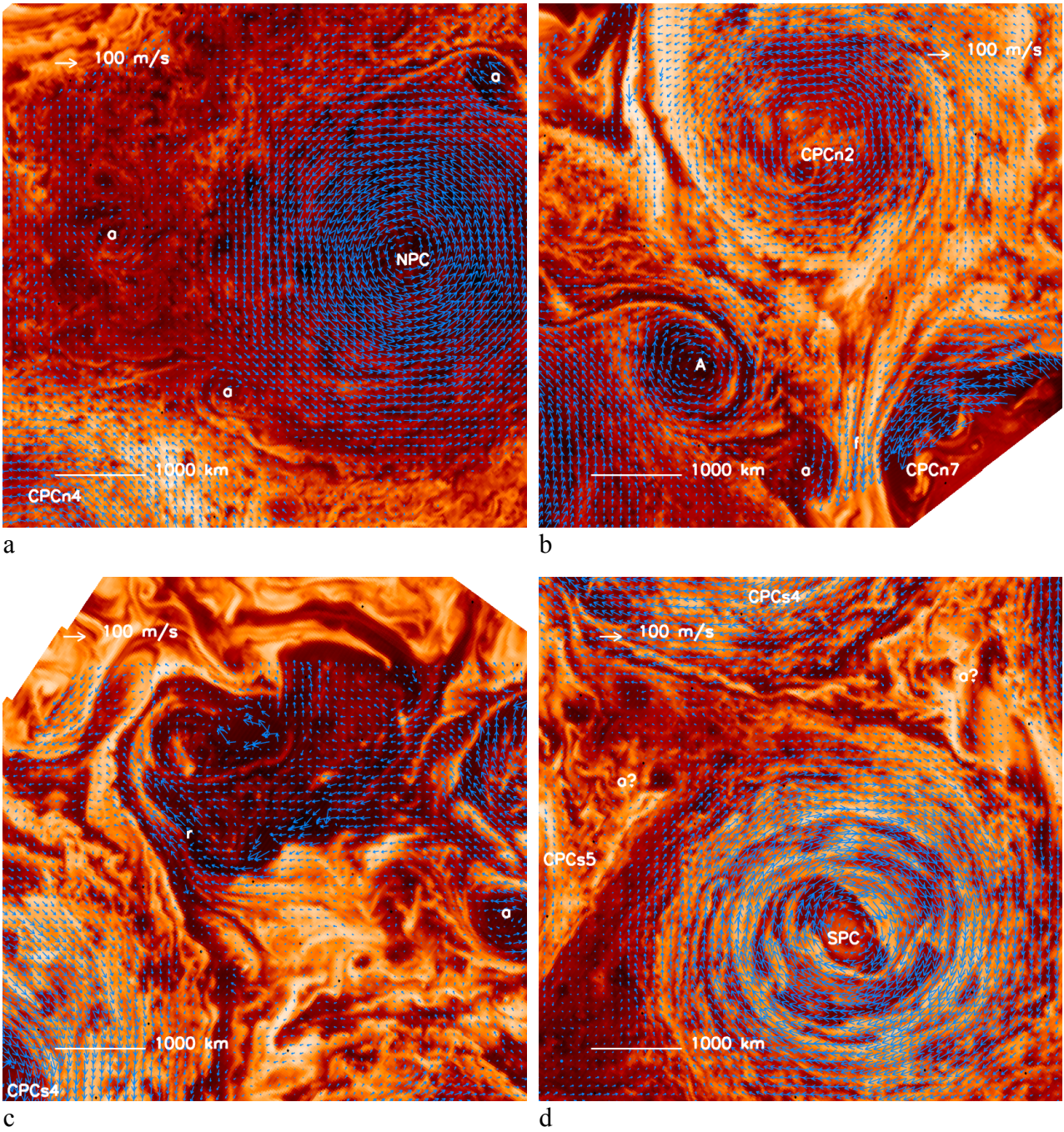
Figure 7. Details from speed fields N1 (panels a and b) and S2 (panels c and d). "A" and "a" letters indicate anticyclonic areas. "a?" indicate possible locations of further anticyclonic areas. "f" and "r" indicate other features discussed in the text

665

23
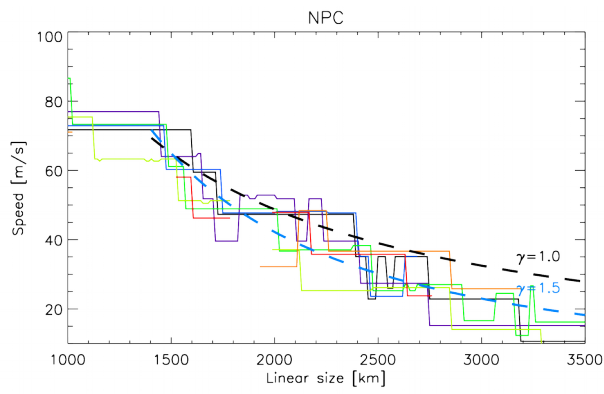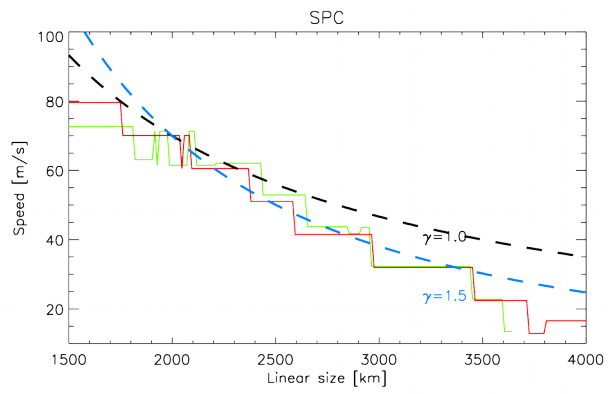
Figure 8. Velocity amplitude profiles vs radius presented in Figure 6 for vortices NPC and SPC are compared against power law profiles $v=c\,r^{-\gamma}$. Panel a: NPC. C_1 is such to provide a speed of 65 m/s at 1500 km from estimated vortex centre. Panel b: SPC. C_1 is such to provide a speed of 70 m/s at 2000 km from estimated vortex centre.

670

Minimum detectable wind: 12 m/s

a
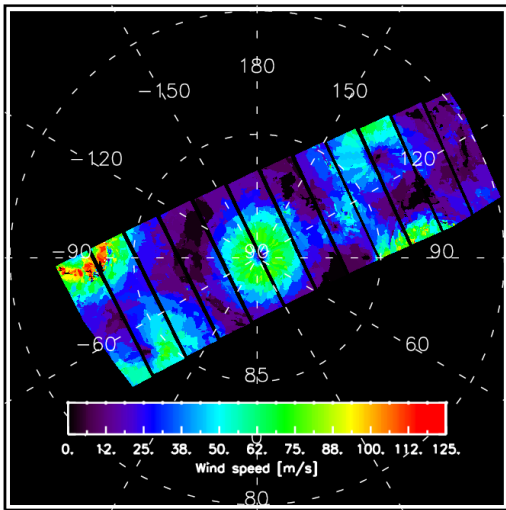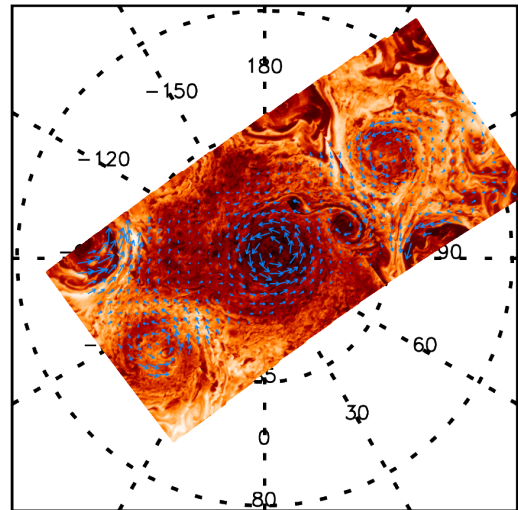
b
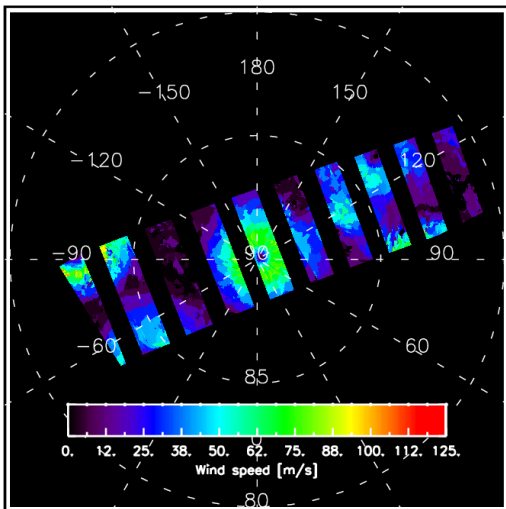
Minimum detectable wind: 12 m/s
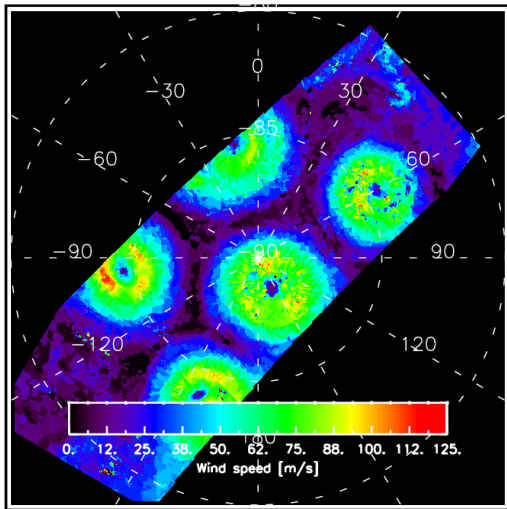
c
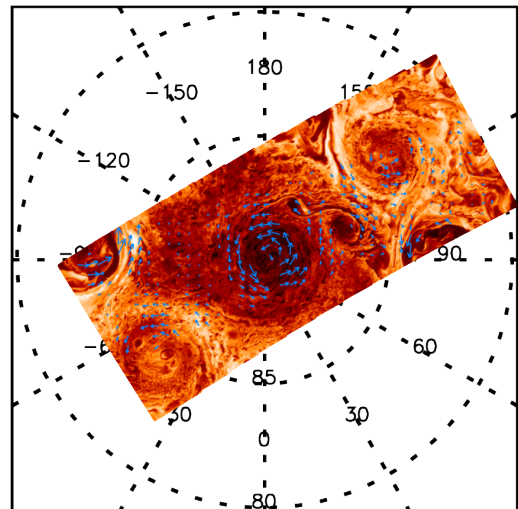
d
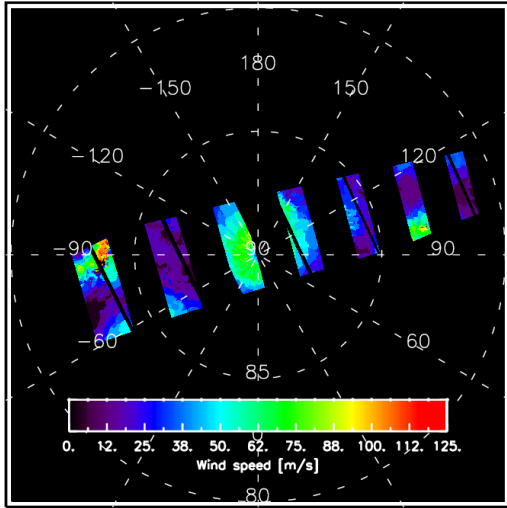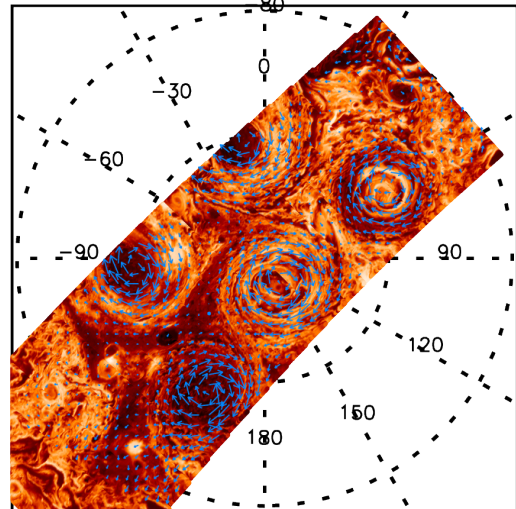
Minimum detectable wind: 12 m/s

e
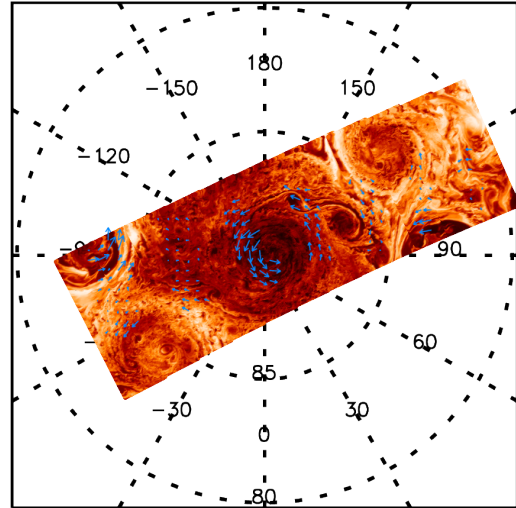
100 m/s

f

Figure A1: Wind velocity amplitudes and directions over the north pole, as corrected to achieve maximum azimuthal symmetry of wind speed around the centre of NPC. Case N2: panels a and b; Case N3: panels c and d; Case N4: panels e and f.

Minimum detectable wind: 9 m/s

a

100 m/s

b

Figure A2: Wind velocity amplitudes and directions over the south pole, as corrected to achieve maximum azimuthal symmetry of wind speed around the centre of SPC. Case S1: panels a and b.
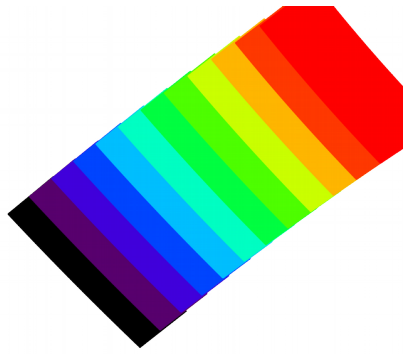
675

26

Figure A3: actual scheme of individual JIRAM images used to build the background image of figures 2b and 3b. Each colour corresponds to a different image inside the sequence 170202_114231. Acquisition times of images were spaced in intervals of 30 seconds.